ADVANCED ENERGY MATERIALS
www.advenergymat.de

Efficient Micrometer Thick Bifacial Perovskite Solar Cells

*Nathan Rodkey, Kassio P. S. Zanoni, Manuel Piot, Chris Dreessen, Roos Grote, Perrine Carroy, Javier Enrique Sebastian Alonso, Abhyuday Paliwal, Delfina Muñoz, and Henk J. Bolink**

Perovskite solar cells have become promising candidates for thin-film photovoltaics (PV), but many record cells suffer from losses in current (≈3–4 mA cm^{-2}). This is due to the choice of superstrate configurations (i.e., glass-side illumination) and thin absorber layers, typically on the order of ≈500 nm. Illumination through a top transparent conductive oxide electrode (substrate configuration) using LiF and Al_2O_x as anti-reflective coatings leads to reflectance losses below 1% is demonstrated. When combined with 1 µm thick absorber layers, substrate configurated bifacial devices have power conversion efficiencies >20%, with minimized reflection losses approaching 98% of their detailed-balance limits and higher Jsc than their monofacial counterparts. Further analysis is conducted to show there is still a significant fraction of current lost due to poor charge-carrier extraction (e.g., resistive or low mobility contacts). This is studied by a direct comparison of photoluminescence at short-circuit versus open-circuit estimating a 4.5% loss in charge-carrier collection.

1. Introduction

Perovskite photovoltaics (PV) have seen a surge in interest over the last decade and recent progress in defect passivation[1,2] and interface control[3–6] have pushed single-junction efficiencies close to those of silicon technologies.[7] This, in combination with their wide versatility in material properties and ease of fabrication, have made them a choice candidate for next generation PV technologies. Most reported perovskite solar cells have used solution-based processes; however, solvent-free alternatives are gaining momentum as perovskite solar cell performance is reaching levels required for first industrial applications. Vacuum techniques offer a promising route to industrialization, with many examples already present in the community of semiconductor and PV manufacturing.[8–10]

Of the potential vacuum techniques for perovskite synthesis, the most widely reported is thermal co-sublimation. This is done by subliming perovskite precursors synchronously, and controlling the stoichiometry by in-situ rate monitoring.[11] Thermal evaporation is a scalable deposition method with demonstrations of high-efficiency on both small- and large- area devices as well as modules.[12–14] A notable advantage of this technique is its additive nature in that there is no processing limit to film thickness, and thermal evaporation sources can be sequentially positioned in a process line to increase deposition speed and/or tune composition.[15] Nevertheless, most solar cells use perovskite thicknesses well below 1 micrometer due to difficulties in processing and in some cases due to limitations in charge carrier diffusion lengths.[16] This limited film thickness has naturally led the community toward superstrate configured devices (i.e., glass-side illumination), employing a reflective top metal electrode as this increases the optical path length. This is mostly needed to increase the absorption of near-bandgap light for thin perovskite layers (<1 µm) and the top metal electrode can be easily applied onto the active stack using thermal sublimation, without significant damage to the perovskite and or charge selective layers in the stack.

The resulting glass/air interface of these superstrate configured devices imposes a challenge for anti-reflection, as perfectly index-matched materials are difficult to come by. This has not stopped the widespread use of anti-reflection coatings (ARC) in perovskite PV, typically relying on illumination from the glass side. In fact, many perovskite solar cells with PCE's >24% and external quantum efficiencies (EQE) >95% were reported with the use of anti-reflective coatings in a superstrate layout (seemingly with single or multi-layer anti-reflective coatings).[17–23]

N. Rodkey, K. P. S. Zanoni, M. Piot, C. Dreessen, R. Grote, J. E. Sebastian Alonso, A. Paliwal, H. J. Bolink
Instituto de Ciencia Molecular
Universidad de Valencia
Calle Catedrático J. Beltrán 2, Paterna 46980, Spain
E-mail: henk.bolink@uv.es
P. Carroy, D. Muñoz
CEA
LITEN
INES
Univ Grenoble Alpes
Grenoble F-38000, France

The ORCID identification number(s) for the author(s) of this article can be found under https://doi.org/10.1002/aenm.202400058

DOI: 10.1002/aenm.202400058

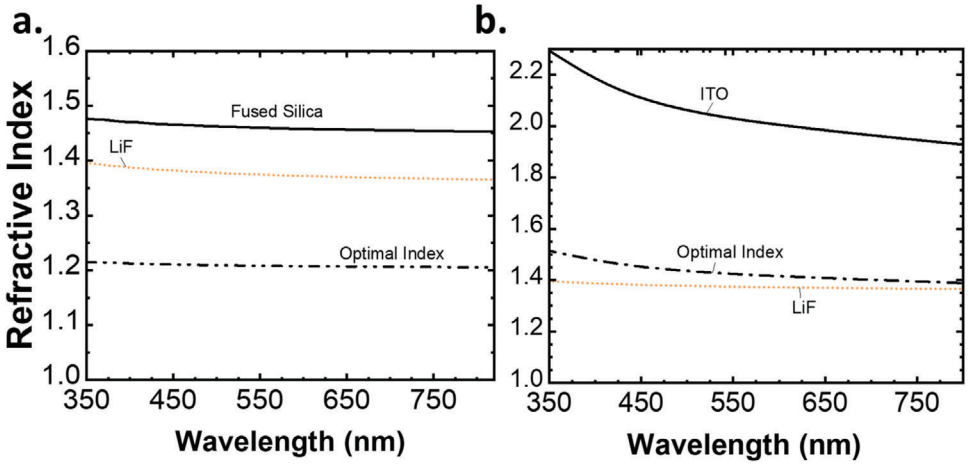

Figure 1. In (a) the measured refractive index of a fused silica (glass) substrate is shown in solid black, with the optimal refractive index needed for anti-reflection between fused silica and air plotted in a black dot-dash line. This optimal index is far from the measured index of common anti-reflective materials such as LiF shown in a dotted orange line. Similarly, in (b) the measured refractive index of ITO (solid black) and the optimal refractive index for a single-layer anti-reflection coating (dot-dash) for the ITO/air interface. Plotted in a dotted orange line is again the refractive index of LiF, this time much closer to the ideal refractive index needed for anti-reflection at the ITO/air interface.

Other groups have investigated better index-matched materials (typically porous coatings) to replace single-layer LiF or MgF_2 anti-reflection coatings but continue to evaluate the scalability of such processes.[24–26] In the silicon/perovskite tandem community, devices are measured in a substrate configuration (top-illumination), with LiF or MgF_2 used as anti-reflection, carefully choosing the thickness of their TCO stacks for both the optical gains and the needed lateral electrical conduction.[27,28]

While perovskites do approach efficiencies competitive with silicon, current market transitions in the silicon PV community have pushed most of production toward bifacial modules, with >70% of silicon modules manufactured in 2023 being bifacial and expected to increase to almost 90% by 2030.[10] This has placed pressure on its thin film counterparts to adapt[29,30] and widened the gap between expected power-generation of perovskite and silicon modules. To adapt, and to target higher power-generation with bifacial perovskite devices, the community has already begun to investigate bifacial perovskite devices.[31–34] Recently, Jiang et. al reported bifacial perovskite devices with efficiencies >23%.[35] However, bifacial perovskite devices reported in the literature still rely heavily on solution-based processes and absorber layers <1 µm, with low bifaciality factors.[35–37]

When transitioning to bifacial devices, the rear metal reflector is replaced by a transparent conductive oxide (TCO) such as indium tin oxide (ITO), effectively reducing the path light travels in the perovskite layer by half. To compensate for this, the thickness of the absorber layer must be increased (>1 µm), something that can be achieved with relative ease using vacuum deposition. In these devices with TCO's as both front and rear electrodes one can illuminate the cells through either one of them. When illuminating through to TCO, that is in the substrate configuration the interface with air changes from glass/air to ITO/air. The ITO/air interface, potentially including some thin encapsulation layers enables the formation of efficient anti-reflection layers with commonly used materials, as we describe in this work.

In this work, we show that expanding the absorber layer thickness from 500 nm to 1 µm allows for the fabrication of bifacial (semi-transparent) devices with greater current collection than their monofacial superstrate counterparts. This is notable given the lack of a metal rear reflector. We conceive a triple-layer ARC coating consisting of only one additional thin film to those already present in the device stack and demonstrate that it leads to devices that have a reflectance approaching the ideal limit. The minimized reflection loss of these devices approach ≈98% of the detailed-balance limit (0.56 mA cm^{-2} of reflection). Lastly, to fully understand the current losses in these device stacks, we evaluate each loss mechanism, observing poor charge-carrier extraction and light transmission as the main limitations, accounting for a summed loss of ≈11% (2.94 mA cm^{-2}).

2. Results and Discussion

When looking for an appropriate candidate for anti-reflection at the glass/air interface, finding properly index-matched materials can be challenging. In **Figure 1a**, the refractive index of fused silica (glass) is displayed, along with the refractive index of LiF (a standard anti-reflective material) in a dotted orange line. Also marked is the optimal refractive index for a single-layer ARC (black dot-dash), calculated as described in the Supporting Information. In Figure 1a, the refractive index at 600 nm for LiF is 1.37 far from the ideal index of 1.21. However, when moving to a bifacial device, and considering illumination from the top, the interface to consider becomes the ITO/air interface. For the ITO/air interface, the index matching of LiF is close to ideal (Figure 1b). Note that the ITO layer itself can promote anti-reflection when appropriate ITO thicknesses are employed allowing us to consider a double-layer ARC coatings comprised of ITO and LiF, using the refractive index of $MAPbI_3$ as the substrate. Moreover, to increase the perovskite solar cell's resilience to moisture, an atomic layer deposited (ALD) layer of Al_2O_x is often deposited on top of the ITO layer allowing for triple-layer ARC coating comprised of ITO/Al_2O_x/LiF. The ideal refractive indices of a double- and triple-layer ARC coating using $MAPbI_3$ as the substrate are shown in Figure S1 (Supporting Information) alongside the

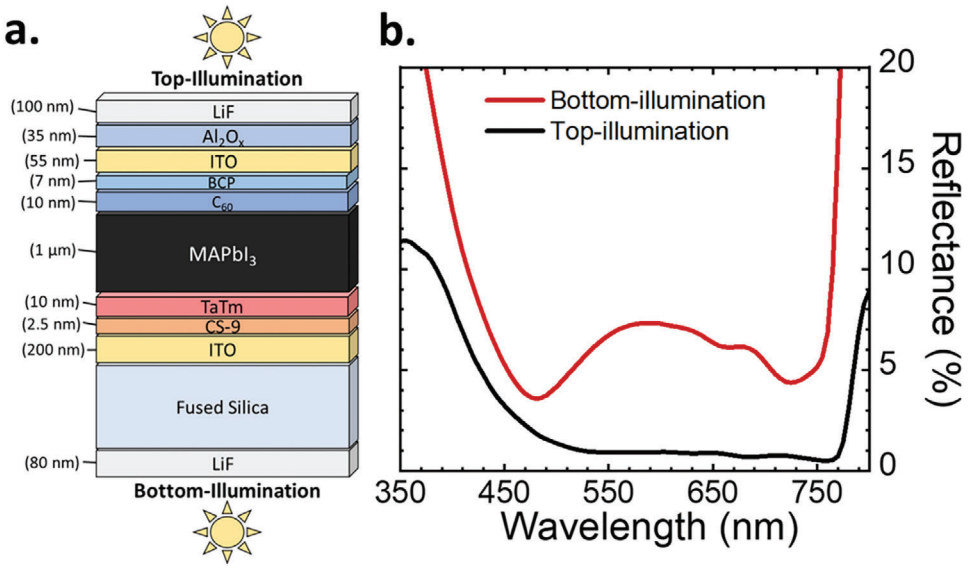

Figure 2. The device architecture of an optimized bifacial device stack is shown in (a). with the measured reflectance shown from top- (black) and bottom-illumination (red) shown in (b). Reflectance from the top is significantly lower, in accordance with the better index-matched anti-reflective coatings explained in Figure 1 and simulated in Figure S3 (Supporting Information). Information on the device stack and materials used are described in the Experimental Section.

measured indices of ITO, LiF, and Al_2O_x. Similarly, this is shown for a fused silica substrate (Figure S2, Supporting Information). These simulated coatings do not include the charge transport layers that we consider to be sufficiently thin as to have a small effect on the reflective properties of the stack, allowing us to focus on the ideal limits of the ARC coatings. The potential benefits of a double-layer ARC employing solely ITO/LiF or a triple-layer coating using ITO/Al_2O_x/LiF are evidenced by the proximity of their indices to optimally index matched materials. It is important to emphasize that the ITO and Al_2O_x layers are functional coatings, in that they are necessary for providing charge transport and encapsulation,[38] requiring only one additional LiF step to complete the stack and thus allowing for ease of integration.

We proceeded to optimize a triple-layer ARC by varying the LiF thickness on the stack, choosing to fix the ITO thickness at 55 nm to ensure proper electrical performance and transparency as well as the Al_2O_x thickness at 35 nm to reduce the process times for the ALD step, as described in the Experimental Section. In **Figure** 2a, the optimized bifacial device stack is shown alongside its measured reflectance using top- and bottom-illumination in Figure 2b. When integrated under AMG1.5, the optimized device stack had a reflectance of 0.56 mA cm^{-2} in a substrate configuration (top-illumination). The reflectance of stacks with varying LiF thickness can be found in Figure S3 (Supporting Information) where it is seen that by increasing the LiF thickness beyond 100 nm the reflectance improves in the 550 to 650 nm range, bringing it near 0%, but an interference fringe in the UV wavelengths (marked by a black arrow) causes significant current loss. Additionally, moving to lower thicknesses pushes the offset of the reflectance from 1% to ≈2–3% in the 550 to 750 nm range. The reflectance of samples with 110 nm ITO layers (more suitable for large-area devices) were also evaluated and shown to perform only slightly worse than their 55 nm ITO counterparts (0.18 mA cm^{-2} increase in reflectance; AMG1.5) and still significantly better than the superstrate configurated devices, with an 0.74 mA cm^{-2} current loss due to reflectance for an optimal LiF thickness of 80 nm (Figure S4b, Supporting Information). Additionally, double-layer coatings of ITO/LiF were measured to understand the importance of the Al_2O_x encapsulation layer on the anti-reflective properties and found to have similar reflectance when reducing the LiF layer to 80 nm, with a difference in integrated reflectance of only 0.02 mA cm^{-2} (Figure S5, Supporting Information) to its ITO/Al_2O_x/LiF counterpart. However, as the Al_2O_x encapsulation layer is necessary for the device fabrication, we report all devices in this work with a triple-layer ARC stack.

In Figure S6 (Supporting Information), transfer-matrix simulations[39,40] were used to calculate the ideal reflectance expected at each interface. This was done by using the optimal refractive index and a combination of thicknesses that led to the smallest integrated current under AMG1.5, as described in the Experimental Section. The minimized ideal reflectance equated to losses in current-density in the solar cell of 0.76 and 0.17 mA cm^{-2} for an ideal superstrate (bottom-illumination) and ideal substrate (top-illumination) configuration respectively. When comparing the experimental results for the top illuminated ARC (Figure 2b) the calculated reflectance loss of 0.56 mA cm^{-2} outperforms an ideal single-layer anti-reflective case for superstrate configurated devices.

This reduced reflectance for top-illuminated devices is promising, but the removal of a metal rear reflector causes severe current-loss from an increase in light transmission. In a 500 nm bifacial (semi-transparent) $MAPbI_3$ device, this loss is calculated to be 3.12 mA cm^{-2}. This loss in transmitted light outweighs the gains in reduced reflectance. Thus, an increase in the absorber layer thickness is required. We evaluate devices in which the absorber layer was increased to 1 µm, both in bifacial

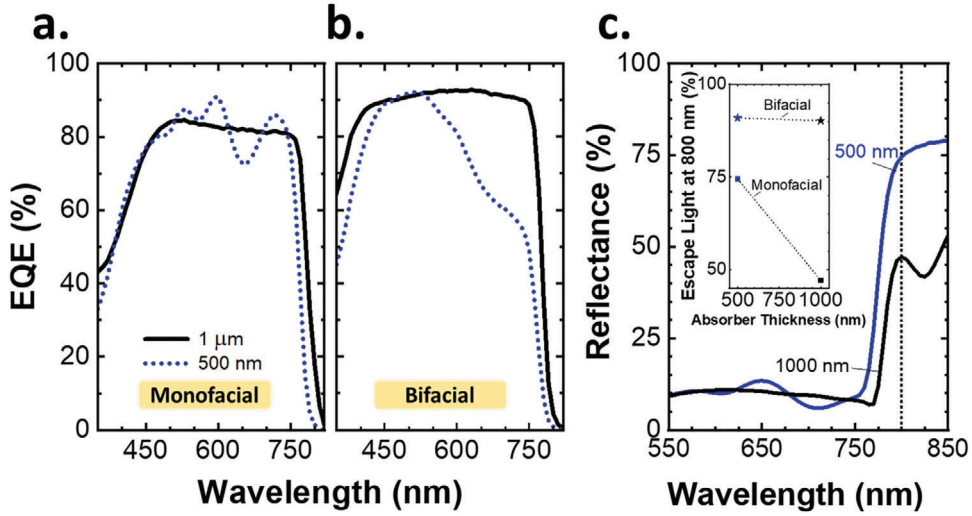

Figure 3. In (a) the EQE for a bottom-illuminated monofacial (opaque) device with a perovskite layer of 500 nm (blue dotted line) and 1 µm (black solid line) and b) the EQE for a top-illuminated bifacial (semitransparent) device with a perovskite layer of 500 nm (blue dotted line) and 1 µm (black solid line). In (c) the reflectance as a function of wavelength for monofacial devices with a perovskite layer of 500 nm (blue) and 1 µm (black). A vertical dotted line is drawn at 800 nm where a reduction in reflectance at 800 nm is apparent, indicating reduced escape reflectance. In the inset the total reflectance of monofacial (squares) and the summed reflectance and transmittance of bifacial devices (stars) at 800 nm is shown.

(semi-transparent) and monofacial (opaque) cells. In **Figure 3** the EQE for cells with absorber layer thicknesses of 500 (blue) and 1 µm (black) are displayed; the exact solar cell stack is described in more detail in the Experimental Section. An increase in infrared absorptance is seen when increasing the absorber layer thickness for both device architectures (Figure 3a,b). This amounts to a 0.26 mA cm^{-2} gain in short-circuit current (J_{sc}) for the monofacial case. Also seen is the removal of interference fringes in the monofacial case (Figure 3a). This is surprising as both the thin bottom ITO (200 nm) and $MAPbI_3$ should induce some degree of interference. A possible explanation is in the roughness of the device stack, which can be observed in an SEM cross-sectional image provided in Figure S7 (Supporting Information) and where a significant influence on the optical length can be observed for light normal to the surface (Figure S7b, Supporting Information). A reduction in the reflectance (e.g., escape reflectance) at 800 nm when moving to thicker films can be seen in Figure 3c. This is also shown in the inset (squares) of Figure 3c. This is caused by an increased absorption in the film. The inset of Figure 3c depicts the summed reflectance and transmittance of a 500 nm and 1 µm bifacial stack (stars), which nears 90% for both, correlating well to the lower near bandgap absorption expected when removing the rear metal reflector. The difference between the escape reflectance of a 1 µm bifacial stack and a 500 nm monofacial stack (whose optical lengths are identical) can be attributed to the increased absorption of infrared light by the TCO in the monofacial device, and the positioning of interference fringes.

Notably, in Figure 3a,b an offset between the monofacial and bifacial EQE's can be observed, caused by the reduced reflectance in the substrate configuration. The collection in the ultraviolet (UV) region is different between the device configurations, with the monofacial stack collecting significantly less light. This has to do with the ITO coated substrate used, whose transmittance is significantly lower than the optimized ITO recipes used in this work for depositing the top electrode of bifacial stacks. However, both the bifacial and monofacial device configurations employ the same patterned ITO substrates; the effect is not observed in the bifacial configuration because the UV light does not reach the TCO on the backside.

This can be promising for the upscaling of such devices, as the optical properties of the bottom TCO become less significant. For example, devices with two bottom TCO's (an ITO reference, 200 nm thick, and a more absorbing FTO substrate, 320 nm thick) were fabricated and the EQEs of bifacial (top-illumination) (**Figure 4**a) and monofacial (Figure 4b) devices were checked. Their absorptances are shown in Figure S8 (Supporting Information), alongside the absorptance of the top ITO electrode. The EQE's of such devices, when measured from the glass-side show notable differences attributed to the choice of TCO. However, when measured from the top, no such difference is observed with the integrated J_{sc} shown to be 23.45 and 23.13 mA cm^{-2} for FTO and ITO devices respectively. This allows for more freedom with the bottom TCO and greater potential for large-area devices where thicker and more conductive TCO's are desired. The EQE current mismatch of an ITO-device amounts to 3.42%. Finally, in Figure 4c the average JV curve for 1 µm devices are shown with substrate versus superstrate illumination, compared to a 1 µm thick monofacial device. Each curve is averaged from eight devices on one substrate. All devices exhibit little hysteresis, and the stabilized efficiency (≈1000 s) and JV sweep of an exemplary device is shown in Figure S9 (Supporting Information). In Figure S10 (Supporting Information) the dark JV curve of this device is also reported. A notable increase in current of 1.01 mA cm^{-2} is observed when comparing the top-illuminated bifacial device to its monofacial counterpart. The champion device exhibited a PCE of 20.06% (Figure S11, Supporting Information). The stability of similar monofacial devices employing the same perovskite has been reported previously.[48] Preliminary stability data indicate that the stability of bifacial devices is independent with respect

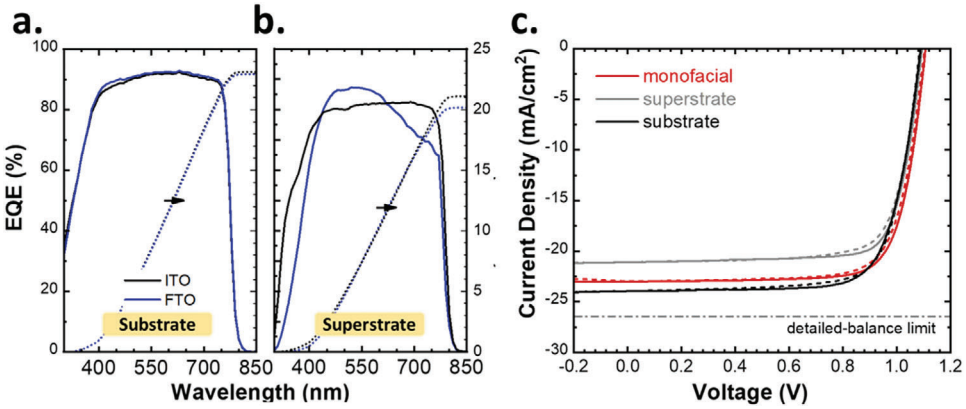

Figure 4. Solar devices with absorber layers 1 µm thick were fabricated and characterized. In (a) the top-illuminated (substrate) EQE's of two device stacks, one with FTO (blue) and the other with ITO (black) are shown with their integrated current under AMG1.5 shown in dotted lines. In (b) the EQE's of these same devices are shown but with illumination from the glass-side (superstrate). A notable decrease is observed caused by increased reflection, as well as an asymmetry between the two EQE's, caused by the different reflection and absorption of the corresponding TCO substrates. Measured from the bottom, the integrated current approaches 23.2 mA cm^{-2} for these top-illuminated devices. In c. the average forward (dash) and reverse (solid) JV curves for an ITO device are shown measured with top- versus bottom-illumination (substrate vs superstrate). Also shown is its monofacial equivalent employing the same ITO. JV curves are each an average of eight devices, 1 substrate. Plotted in a dot-dash line is the detailed balance limit of the current-density assuming a step-function for absorption starting at 800 nm.

to the way the devices are operated. In Figure S13 (Supporting Information), JV curves for two types of devices are shown when stressed at 85 °C for 96 h operated in substrate and superstrate configuration (that is illuminated toward the top TCO or toward the bottom TCO). For both pixel sizes no notable difference between the illumination direction can be observed. The cells with an active area of 0.25 cm^2 show virtually no degradation over this time period, whereas the 1 cm^2 devices increase when held at 85 °C for 96 h.

We comprehensively study the origin of such losses in **Figure 5**. The 1-reflectance (R) and absorptance (A) are plotted alongside the EQE to fully understand where the current losses occur. Notably, the reflectance loss has been reduced to 0.56 mA cm^{-2}, meaning that ≈98% of the light (integrated below 800 nm; AMG1.5) enters the device. Parasitic absorption in the UV and infrared are attributed to absorption in the contacts and ITO but amount to an insignificant fraction of the total light. Instead, the main losses occur in the transmitted light (1.6 mA cm^{-2}) and internal current collection losses (1.27 mA cm^{-2}). Unfortunately, transmitted light cannot be better collected without fundamentally increasing the absorption coefficient of the perovskite absorber layer or by increasing the optical path length of the incoming light. The latter could be done by increasing the optical roughness or increasing the absorber layer thickness. Internal collection loss was estimated as 4.5% (explained in detail in the following section) by a series of open-circuit and short-circuit PL measurements. We note a constant offset between the 1-R and the EQE, relatively independent of wavelength, that indicate collection losses at the contacts as opposed to poor diffusion lengths.

This can be seen in the internal quantum efficiency (IQE) (**Figure 6**) of such a device, where a constant offset of ≈5–7% over the 400–750 nm wavelength range is observed, indicating that charges are not completely extracted from the device. To corroborate this charge-extraction loss, we collect the photoluminescence of devices at short-circuit (PL_{OC}) and open-circuit (PL_{SC}), shown in the inset of Figure 6.[41–43] As expected, the PL is much higher in open-circuit than in short-circuit as in open-circuit all excited carriers must eventually recombine (either radiatively or trap-assisted). However, in short-circuit conditions, charges prefer to flow into the external circuit and recombine without luminescing. This charge-current represents the J_{SC} of a stereotypical PV device. However, not all excited carriers reach the external circuit, which leads to a small, but noticeable, PL signal, as well as a loss in J_{SC}. By using the ratio between the open-circuit PL (ϕ_{OC})

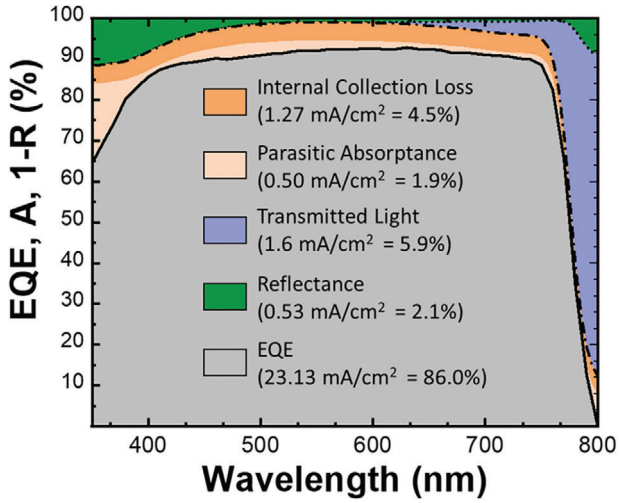

Figure 5. Losses in a bifacial device (top-illumination) are evaluated by plotting the absorptance (A, dot-dash line), 1-reflectance (1-R, dotted line), and EQE (solid line) of this device. Notable, the low 0.56 mA cm^{-2} reflection losses. The main current losses occur instead in the transmitted light (1.6 mA cm^{-2}) shaded in blue and the internal collection loss (1.27 mA cm^{-2}) shaded in dark orange. An estimate for the blue and IR parasitic absorption caused by losses in the ITO and charge transport layers are shaded in light orange.

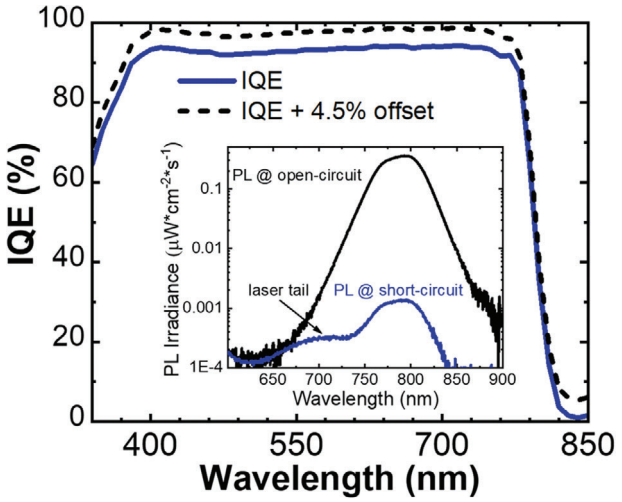

Figure 6. The internal quantum efficiency (IQE) is shown above. The relatively flat offset of 5–7% is an indication of poor internal collection efficiency, which we evaluate by measuring the PL at open-circuit and short-circuit conditions (shown in inset). A 4.5% carrier-collection loss is estimated in this way, attributed to resistive contacts.

and the short-circuit PL (ϕ_{SC}) we can estimate the internal collection loss, calculated using Equation (1):

$$\left(\frac{\phi_{SC}}{\phi_{OC}}\right)^{\frac{1}{n_{id}}} = \frac{\Delta J_{sc}}{J_L} = \%\ internal\ collection\ loss \quad (1)$$

where n_{id} is the ideality factor, ΔJ_{sc} is the current loss in mA cm^{-2}, and J_L is the generated carriers by illumination in mA cm^{-2}. The PL_{SC} and PL_{OC} curves were integrated, and the ideality constant was estimated using the linear fit of intensity-dependent V_{OC}. Due to the low intensity of PL_{SC} a peak from the laser tail is observed. This peak is subtracted as a background before performing the integration. In this way, the final % internal collection loss was estimated to be 4.5% ($\sigma = 0.272\%$; estimated from fit of ideality constant). To better visualize this loss, we have added a 4.5% offset in a dashed line to Figure 6. As the curve never quite reaches 100%, we can assume the unaccounted-for losses come from parasitic absorption, also visualized in Figure 5 (shaded in light orange)

3. Conclusion

In this work, we show remarkably low reflection (0.56 mA cm^{-2}) of an exemplary perovskite solar, whose champion PCE reaches 20.06%, competitive with current reflection losses in world record devices. We argue that this has to do with switching to a substrate configured bifacial device due to the increased availability of anti-reflective material. By properly choosing the thickness of a ITO/Al_2O_x/LiF stack, the bifacial device can outperform its monofacial counterpart, which is significant considering the lack of a metal rear-reflector. This increased performance is only observed when moving from 500 nm to 1 μm thick absorber layers, due to the increased transmission of infrared light experienced by bifacial devices. We also point out the benefits of such configured devices, which no longer experience parasitic losses from the bottom TCO layer, with evident benefits for large-area devices where thick, conductive TCO's, or reduced metallization is needed. With increased interest in both perovskite- and Si-based solar cells for bifacial PV, we think this is an important step in understanding light management in bifacial perovskite solar cells.

4. Experimental Section

The transfer matrix method used for optical simulations in this work was adapted from open-source code provided by Dr. Koen Vandewal. A link to the code is also provided in the Supporting Information. The basic function of the program is as follows: a stack of materials with known n&k was defined, a thickness for these materials was defined, and finally each material was defined as coherent or incoherent layers. A transfer-matrix was then used to calculate the transmission and reflection of the stack, as well as the absorption of each individual layer. For simulations estimating the ideal thicknesses of anti-reflective layers, the perovskite layer was assumed to be infinitely thick and incoherent. Additionally, ideal ARC coatings were calculated by using the optimal refractive index of each coating and subsequently iterating through a matrix of possible thicknesses. In this matrix, the ITO thickness minimum was set to 50 nm, as a minimum thickness is required to maintain proper electrical conduction. The combination of thicknesses with the lowest reflectance (integrated over AMG1.5) was then designated as the optimum.

A Jobin Yvon Horiba Spectroscopic ellipsometer was used to extract the refractive indices and absorption coefficients of TCOs using a Drude–Lorentz model.[44] For the dielectric layers (LiF and Al_2O_x), the fitting of ellipsometry spectra to obtain the optical constants used an amorphous dispersion formula developed by Horiba Jobin Yvon based on the Forouhi–Bloomer dispersion formula, suitable for highly transparent materials.[45]

Device fabrication was as follows. Patterned ITO glass bought from an external provider, with a thickness of 200 nm was used as the substrate for all devices reported here unless otherwise stated. A hole-transport material consisting of CS-9 ((2,2′,2″-(cyclopropane-1,2,3-triylidene)tris(2-(pcyanotetrafluorophenyl)acetonitrile) and Tatm ((N4,N4,N4″,N4″-tetra([1,1′-biphenyl]−4-yl)-[1,1′:4′,1″-terphenyl]−4,4″-diamine) of 2.5 and 10 nm respectively was deposited by thermal evaporation. Next, the perovskite absorber layer ($MAPbI_3$) was deposited by thermal co-evaporation of MAI and PbI_2 sources.[15,46] Subsequent thermal evaporation of C_{60}/BCP (bathocuproine) contacts of 10 and 7 nm were used as the electron transport layer (ETL). For bifacial devices, a soft-deposition of ITO by pulsed laser deposition was used, as described in a previous work by Zanoni et al,[47] before finishing the device with evaporated Ag electrodes. Finally, the devices are encapsulating using an ALD Al_2O_x process,[48] and a LiF layer was evaporated onto the now encapsulated devices.

Finished devices were then illuminated in air under a Wavelabs Sinus 70 AAA LED solar simulator. Illumination intensity was calibrated to 1-sun before each measurement using a calibrated Si reference diode, equipped with an infrared cutoff filter (KG-5, Schott). A mismatch factor of 1.011 was calculated using the spectral irradiance of AMG1.5 and the LED simulator compared to the EQE of the reference cell and a $MAPbI_3$ solar cell (Figure S12 and Equation S13, Supporting Information). Devices had a total area of 0.0825 cm^2 and an illuminated area of 0.05 cm^2, defined through the use of metal shadow masks during the deposition and measurement process. Devices were kept at open-circuit for 10 s before a voltage sweep from −0.2 to 1.2 V, with a scan speed of 0.5 V s^{-1}. Reflectance, transmittance, and absorptance measurements were collected using a PerkinElmer Lambda 950 UV–vis- NIR spectrometer. This system is coupled to an integrating sphere. External quantum efficiency (EQE) was measured using a system developed by QE-R by Enli Technology Co., Ltd. Photoluminescence (PL) was measured at steady-state, using a custom-built system calibrated with an Avantes cosine corrected lamp of known intensity. Devices were measured at open-circuit and short-circuit conditions using a 522 nm excitation laser.

Supporting Information

Supporting Information is available from the Wiley Online Library or from the author.

Acknowledgements

The authors acknowledge financial support of the European Research Council (ERC) under the European Union's Horizon 2020 research and innovation programme (Grant Agreement no. 834431). Funded by the European Union. Views and opinions expressed are however those of the author(s) only and do not necessarily reflect those of the European Union or CINEA. Neither the European Union nor the granting authority can be held responsible for them. NEXUS project has received funding from Horizon Europe Research and Innovation Action programme under Grant Agreement no. 101075330. Authors acknowledge support from the Comunitat Valenciana (MFA/2022/022 and IDI-FEDER/2021/078), as well as from the Ministry of Science and Innovation (MCIN) and the Spanish State Research Agency (AEI): project TED2021-129679B-C21 and grant IJC2020-045130-I funded by MCIN/AEI/10.13039/501100011033 and by the "European Union NextGenerationEU/PRTR"; project CEX2019-000919-M funded by MCIN/AEI/10.13039/501100011033. C.D. acknowledges the support of the fellowship from "la Caixa" Foundation (ID 100010434). The fellowship code is LCF/BQ/DI19/11730020.

Conflict of Interest

The authors declare no conflict of interest.

Data Availability Statement

The data that support the findings of this study are available from the corresponding author upon reasonable request.

Keywords

bifacial, evaporated, perovskite, semi-transparent, solarcells

Received: January 4, 2024
Revised: February 8, 2024
Published online: March 3, 2024

[1] Z. Wu, E. Bi, L. K. Ono, D. Li, O. M. Bakr, Y. Yan, Y. Qi, *Nano Energy* **2023**, *115*, 108731.
[2] Y. Zhou, I. Poli, D. Meggiolaro, F. De Angelis, A. Petrozza, *Nature Res.* **2021**, *6*, 986.
[3] S. Yan, J. B. Patel, J. E. Lee, K. A. Elmestekawy, S. R. Ratnasingham, Q. Yuan, L. M. Herz, N. K. Noel, M. B. Johnston, *ACS Energy Lett.* **2023**, *8*, 4008.
[4] B. Liu, J. Hu, D. He, L. Bai, Q. Zhou, W. Wang, C. Xu, Q. Song, D. Lee, P. Zhao, F. Hao, X. Niu, Z. Zang, J. Chen, *ACS Appl. Mater. Interfaces* **2022**, *14*, 21079.
[5] B. Yang, J. Suo, F. Di Giacomo, S. Olthof, D. Bogachuk, Y. Kim, X. Sun, L. Wagner, F. Fu, S. M. Zakeeruddin, A. Hinsch, M. Gratzel, A. Di Carlo, A. Hagfeldt, *ACS Energy Lett.* **2021**, *6*, 3916.
[6] W. Shen, Y. Dong, F. Huang, Y. B. Cheng, J. Zhong, *Mater. Rep.: Energy* **2021**, *1*, 100060.
[7] *NREL. Best Research-Cell Efficiencies*, https://www.nrel.gov/pv/cell-efficiency.html (accessed: October 2023).
[8] J. P. Spindler, J. W. Hamer, M. E. Kondakova, *OLED Manufacturing Equipment and Methods* in *Handbook of Advanced Lighting Technology*, Springer International Publishing, Berlin, Germany **2017**, pp. 417–441, https://doi.org/10.1007/978-3-319-00176-0_26.
[9] C. A. Miller, I. M. Peters, S. Zaveri, Thin Film CdTe Photovoltaics and the U.S. Energy Transition in *2020*, **2020**.
[10] International Technology Roadmap for Photovoltaic (ITPRV), **2023**, Vol. 14th Editi, https://itrpv.vdma.org/en/ueber-uns.
[11] K. P. S. Zanoni, L. Martínez-Goyeneche, C. Dreessen, M. Sessolo, H. J. Bolink, *Sol. RRL* **2023**, *7*, 2201073.
[12] D. B. Ritzer, T. Abzieher, A. Basibüyük, T. Feeney, F. Laufer, S. Ternes, B. S. Richards, S. Bergfeld, U. W. Paetzold, *Prog. Photovolt.: Res. Appl.* **2022**, *30*, 360.
[13] A. Bruno, A. Di Carlo, U. W. Paetzold, *Solar RRL* **2022**, *6*, 2101046.
[14] F. U. Kosasih, E. Erdenebileg, N. Mathews, S. G. Mhaisalkar, A. Bruno, *Joule* **2022**, *6*, 2692.
[15] M. Piot, J. E. S. Alonso, K. P. S. Zanoni, N. Rodkey, F. Ventosinos, C. Roldán-Carmona, M. Sessolo, H. Bolink, *ACS Energy Lett.* **2023**, *8*, 4711.
[16] T. Soto-Montero, W. Soltanpoor, M. Morales-Masis, *APL Mater.* **2020**, *8*, 110903.
[17] H. Li, J. Zhou, L. Tan, M. Li, C. Jiang, S. Wang, X. Zhao, Y. Liu, Y. Zhang, Y. Ye, W. Tress, C. Yi, *Sci. Adv.* **2022**, *8*, abo7422.
[18] T. Yang, L. Gao, J. Lu, C. Ma, Y. Du, P. Wang, Z. Ding, S. Wang, P. Xu, D. Liu, H. Li, X. Chang, J. Fang, W. Tian, Y. Yang, S. Liu, K. Zhao, *Nat. Commun.* **2023**, *14*, 839.
[19] H. Min, D. Y. Lee, J. Kim, G. Kim, K. S. Lee, J. Kim, M. J. Paik, Y. K. Kim, K. S. Kim, M. G. Kim, T. J. Shin, *Nature* **2021**, *598*, 444.
[20] Z. Xie, Y. Do, S. J. Choi, H. Y. Park, H. Kim, J. Kim, D. Song, T. Gokulnath, H. B. Kim, I. W. Choi, Y. Jo, D. S. Kim, S. Y. Yoon, Y. R. Cho, S. H. Jin, *J. Mater. Chem. A* **2023**, *11*, 9608.
[21] J. Jeong, M. Kim, J. Seo, H. Lu, P. Ahlawat, A. Mishra, Y. Yang, M. A. Hope, F. T. Eickemeyer, M. Kim, Y. J. Yoon, I. W. Choi, B. P. Darwich, S. J. Choi, Y. Jo, J. H. Lee, B. Walker, S. M. Zakeeruddin, L. Emsley, U. Rothlisberger, A. Hagfeldt, D. S. Kim, M. Grätzel, J. Y. Kim, *Nature* **2021**, *592*, 381.
[22] G. Kim, H. Min, K. S. Lee, D. Y. Lee, S. M. Yoon, S. I. Seok, *Science* **2020**, *370*, 108.
[23] J. Chen, H. Dong, J. Li, X. Zhu, J. Xu, F. Pan, R. Xu, J. Xi, B. Jiao, X. Hou, K. Wei Ng, S. P. Wang, Z. Wu, *ACS Energy Lett.* **2022**, *7*, 3685.
[24] P. Firth, Z. C. Holman, *ACS Appl. Nano Mater.* **2018**, *1*, 4351.
[25] Q. Luo, X. Deng, C. Zhang, M. Yu, X. Zhou, Z. Wang, X. Chen, S. Huang, *Solar Energy* **2018**, *169*, 128.
[26] M. Spence, R. Hammond, A. Pockett, Z. Wei, A. Johnson, T. Watson, M. J. Carnie, *ACS Appl. Energy Mater.* **2022**, *5*, 5974.
[27] S. Mariotti, E. Köhnen, F. Scheler, K. Sveinbjörnsson, L. Zimmermann, M. Piot, F. Yang, B. Li, J. Warby, A. Musiienko, D. Menzel, F. Lang, S. Keßler, I. Levine, D. Mantione, A. Al-Ashouri, M. S. Härtel, K. Xu, A. Cruz, J. Kurpiers, P. Wagner, H. Köbler, J. Li, A. Magomedov, D. Mecerreyes, E. Unger, A. Abate, M. Stolterfoht, B. Stannowski, R. Schlatmann, et al., *Science* **2023**, *381*, 63.
[28] X. Y. Chin, D. Türkay, J. Steele, S. Tabean, S. Eswara, M. Mensi, P. Fiala, C. M. Wolff, A. Paracchino, K. Artuk, D. Jacobs, Q. Guesnay, F. Sahli, G. Andreatta, M. Boccard, Q. Jeangros, C. Ballif, *Science* **2023**, *381*, 59.
[29] A. B. Phillips, K. K. Subedi, G. K. Liyanage, F. K. Alfadhili, R. J. Ellingson, M. J. Heben, *ACS Appl. Energy Mater.* **2020**, *3*, 6072.
[30] D. Pokhrel, X. Mathew, K. K. Subedi, A. Patel, A. B. Phillips, E. Bastola, A. Abudulimu, M. K. Jamarkattel, S. Rijal, A. Quader, J. Friedl, Z. Zawisza, Y. Yan, M. J. Heben, R. J. Ellingson, *Sol. RRL* **2022**, *6*, 2200501.
[31] P. Kumar, G. Shankar, B. Pradhan, *Appl. Phys. A* **2023**, *129*, 63.
[32] Z. Song, C. Chen, C. Li, S. Rijal, L. Chen, Y. Li, Y. Yan, *Sustainable Energy Fuels* **2021**, *5*, 2865.

[33] Z. Song, C. Li, L. Chen, Y. Yan, *Adv. Mater.* **2022**, *34*, 2106805.
[34] F. Gota, S. X. An, H. Hu, B. Abdollahi Nejand, U. W. Paetzold, *Adv. Opt. Mater.* **2023**, *11*, 2201691.
[35] Q. Jiang, Z. Song, R. C. Bramante, P. F. Ndione, R. Tirawat, J. J. Berry, Y. Yan, K. Zhu, *Joule* **2023**, *7*, 1543.
[36] D. Chen, S. Pang, L. Zhou, X. Li, A. Su, W. Zhu, J. Chang, J. Zhang, C. Zhang, Y. Hao, *J. Mater. Chem. A* **2019**, *7*, 15156.
[37] F. Fu, T. Feurer, T. Jäger, E. Avancini, B. Bissig, S. Yoon, S. Buecheler, A. N. Tiwari, *Nat. Commun.* **2015**, *6*, 8932.
[38] K. P. S. Zanoni, A. Paliwal, M. A. Hernández-Fenollosa, P. A. Repecaud, M. Morales-Masis, H. J. Bolink, *Adv. Mater. Technol.* **2022**, *7*, 2101747.
[39] K. Bittkau, T. Kirchartz, U. Rau, *Opt. Express* **2018**, *26*, A750.
[40] A. Bojar, D. Micha, M. Giteau, M. A. Ruiz-Preciado, U. W. Paetzold, M. Simor, V. S. Gevaerts, R. Carron, K. Medjoubi, S. Collin, N. Naghavi, J. F. Guillemoles, P. Schulz, *JPhys Energy* **2023**, *5*, 035001.
[41] K. Tvingstedt, O. Malinkiewicz, A. Baumann, C. Deibel, H. J. Snaith, V. Dyakonov, H. J. Bolink, *Sci. Rep.* **2014**, *4*, 6071.
[42] U. Rau, V. Huhn, B. E. L Pieters, *Phys. Rev. Appl.* **2020**, *14*, 014046.
[43] T. Du, W. Xu, S. Xu, S. R. Ratnasingham, C. T. Lin, J. Kim, J. Briscoe, M. A. McLachlan, J. R. Durrant, *J. Mater. Chem. C* **2020**, *8*, 12648.
[44] A. Valla, P. Carroy, F. Ozanne, D. Muñoz, *Sol. Energy Mater. Sol. Cells* **2016**, *157*, 874.
[45] A. R. Forouhi, I. Bloomer, *Phys. Rev. B* **1986**, *34*, 7018.
[46] K. P. S. Zanoni, L. Martínez-Goyeneche, C. Dreessen, M. Sessolo, H. J. Bolink, *Sol. RRL* **2023**, *7*, 2201073.
[47] K. P. S. Zanoni, A. Paliwal, M. A. Hernández-Fenollosa, P. A. Repecaud, M. Morales-Masis, H. J. Bolink, *Adv. Mater. Technol.* **2022**, *7*, 2101747.
[48] I. C. Kaya, K. P. S. Zanoni, F. Palazon, M. Sessolo, H. Akyildiz, S. Sonmezoglu, H. J. Bolink, *Adv. Energy Sustainabil. Res.* **2021**, *2*, 2000065.